KSCE Journal of Civil Engineering (2020) 24(5):1509-1523
DOI 10.1007/s12205-020-0680-3

pISSN 1226-7988, eISSN 1976-3808
www.springer.com/12205

Structural Engineering

Hysteretic Mechanical Behaviour of an Eccentrically Loaded Partially-Concrete-Filled Steel Tubular Bridge Pier under Out-of-Plane Horizontal Cyclic Loading

Weining Sui[a], **Hang Li**[b], **Qiang Zhang**[b], **and Zhanfei Wang**[b]

[a]*School of Civil Engineering, Shenyang Jianzhu University, Shenyang 110168, China*
[b]*School of Transportation Engineering, Shenyang Jianzhu University, Shenyang 110168, China*

ARTICLE HISTORY

Received 19 April 2019
Revised 1 February 2020
Accepted 13 February 2020
Published Online 7 April 2020

KEYWORDS

Hysteresis performance
Eccentrically loaded
Steel tubular bridge pier
Out-of-plane
Concrete-filled
Experimental
Finite element analysis

ABSTRACT

To investigate the hysteretic behaviour of an eccentrically loaded partially-concrete-filled steel tubular (PCFST) bridge pier in an out-of-plane horizontal direction, a quasi-static experiment and finite element (FE) analysis of steel tubular columns were carried out. In this study, four PCFST column specimens were tested under constant eccentrically loaded and out-of-plane horizontal cyclic loading. The elasto-plastic behaviour and failure mode of these specimens were investigated. Secondly, the FE models of these four experimental PCFST columns were established, through comparisons with the experimental results, the validity of the selected elements, mesh division, the contact relationship between the concrete and the steel pipe, and the boundary conditions of FE models were verified. Thirdly, 30 FE models of PCFST bridge piers were analyzed to ascertain the effects of slenderness ratio λ, radius-thickness ratio R_t, and vertical load eccentricity ratio e/L on ultimate strength and ductility. Finally, an empirical formula was proposed to describe the ultimate strength and ductility of such bridge piers for engineering application under complicated loading conditions.

1. Introduction

Steel bridge piers, which have excellent mechanical properties and seismic performance, have been widely used in viaducts and beltways around the world, however, damage to steel bridges, such as local buckling and ductile fracture, occurred in the superstructure and substructure in the 1994 Northridge earthquake, the 1995 Kobe earthquake, the 2008 Wenchuan earthquake, and the 2016 Kumamoto earthquake (Japan Society of Civil Engineers, 1996; Chen and Duan, 2014; Japan Road Association, 2018). In recent studies, various bridge piers have been proposed to improve the seismic performance of bridge piers (Nishikawa et al., 1998; Yamao et al., 2002; Wang et al., 2011; Skalomenos et al., 2016; Zhao et al., 2018; Mahdavi et al., 2019) following the 1995 Kobe earthquake. Little damage to the partially-concrete-filled steel bridge pier of Han-shin highway viaduct was observed during, and after, the Kobe earthquake (Japan Society of Civil Engineers, 1996): the high bearing capacity and ductility arising as a result of the use of in-filled concrete can prevent development of local buckling deformation in steel bridge piers, as evinced by both experiment and numerical analysis (Usami and Ge, 1994; Usami et al., 1997; Ge and Usami, 1996; Iura et al., 2002; Michel and Julia, 2004; Goto et al., 2010, 2012, 2014; Hua et al., 2014; Shimaguchi and Suzuki, 2015; Kim and Shim, 2016).

With the rapid development of modern urban transportation systems, eccentrically loaded steel bridge pier columns, such as the inverted L-shaped bridge piers and frame bridge piers of viaducts, and bridge piers in curved bridges, have appeared in viaducts and beltways (Fig. 1). Eccentrically loaded bridge piers are subjected to pressure, bending, shear, and torsion. This combined action is caused by the vertical eccentric load from the superstructure and additional seismic action that affects the overall performance of steel bridge piers (Gao et al., 2000a, 2000b). Several researchers (Sakimoto et al., 2002; Aoki et al., 2003; Ge et al., 2003; Hirota et al., 2005) have experimentally, and theoretically, investigated the seismic capacity of eccentrically loaded steel bridge piers. Their work indicates that the bearing

CORRESPONDENCE Zhanfei Wang ZFwang@sjzu.edu.cn School of Transportation Engineering, Shenyang Jianzhu University, Shenyang 110168, China

Fig. 1. Eccentrically Loaded Steel Bridge Pier (the inverted L-shaped bridge pier)

capacity and ductility of eccentrically loaded steel bridge pier columns were greatly decreased along the out-of-plane horizontal direction, and empirical formulae for the ultimate strength and ductility of steel tube bridge piers were provided (Gao et al., 2000b).

The ultimate strength and ductility of axial loaded PCFST bridge pier columns have also been evaluated (Iura et al., 2002; Nie et al., 2012; Kim et al., 2016; Wang et al., 2015, 2016; Sui et al., 2018). If the influence of the ultimate strength and ductility of eccentrically loaded PCFST columns along the out-of-plane direction can be ascertained, it will provide a theoretical foundation from which to broaden application of this type bridge pier.

The objective of this research is to investigate the ultimate strength and ductility of eccentrically loaded PCFST columns along the out-of-plane direction through experimental and numerical analytical methods. In this study, four PCFST column specimens are tested under constant axial eccentric loading and out-of-plane horizontal cyclic loading. Secondly, FE models of the four experimental specimens are established, and validity of these FE models will be verified through comparison with experimental results. Thirdly, 30 FE model PCFST bridge piers are analyzed numerically to ascertain effects of slenderness ratio, radius-thickness ratio, and vertical load eccentricity ratio on their ultimate strength and ductility. Finally, an empirical formula is proposed to describe the ultimate strength and ductility of the bridge piers.

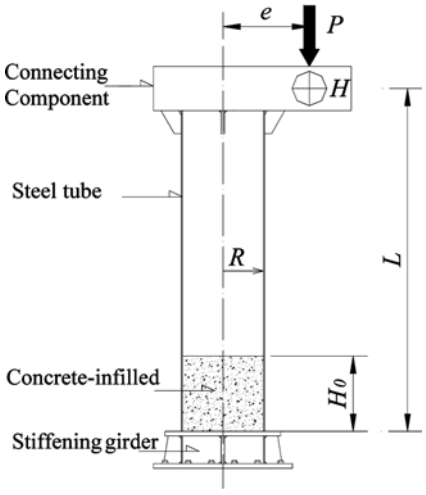

Fig. 2. Test Specimen

2. Experimental Programme

2.1 Test Specimens

In this study, the PCFST inverted *L*-shaped bridge pier is assumed to be a cantilever column, the eccentric compression load and horizontal cyclic load act on top of column along the out-of-plane direction. These four PCFST column specimens are designed according to the test set-up and loading conditions applicable to the laboratory (see Fig. 2). The dimensions of these specimens, and other parameters related, are listed in Table 1, where, L is the vertical distance between the bottom of the column and horizontal loading point, R is the external radius of the steel pier, t is the thickness of the steel tube (5.75 mm), λ is the slenderness ratio of the column, R_t is radius-thickness ratio, H_0 is the concrete in-fill height, ζ is the concrete-filling ratio (H_0/L), e is the horizontal distance between the vertical load and centre of the column, e/L is the eccentricity (0.1), P is the vertical axial load, and P_y is the yield load of the hollow steel tube. The axial compression ratios (P/P_y) are 0.1 and 0.15 in a condition with the same slenderness ratio and radius-thickness ratio. R_t, λ, the theoretical horizontal yield stregnth H_y and the theoretical horizontal yield displacement δ_y are calculated as follows:

$$R_t = \frac{R}{t}\frac{\sigma_y}{E}\sqrt{3(1-\nu^2)} \tag{1}$$

Table 1. Dimensions and Mechanical Parameters of Experimental Specimens

Specimen	L/ mm	R/ mm	λ	R_t	H_0/ mm	$\zeta = H_0/L$	e/ mm	e/L	P/kN	P/P_y
SCP1	1530	150	0.27	0.073	530	0.35	153	0.10	183.4	0.10
SCP2					630	0.41			274.9	0.15
SCP3		180	0.22	0.087	530	0.35			220.8	0.10
SCP4					530	0.35			331.0	0.15

Table 2. Mechanical Property of Steel and Concrete

Material	σ_y/MPa	σ_u/MPa	σ_{cu}/MPa	E/GPa	E_c/GPa	v
Steel	347	506	-	218	-	0.28
Concrete	-	-	51	-	31.062	0.20

$$\lambda = \frac{2L}{\pi r}\sqrt{\frac{\sigma_y}{E}} \tag{2}$$

$$H_y = \frac{\sigma_y I(1-P/P_y)-Pe}{L} \tag{3}$$

$$\delta_y = \frac{H_y L^3}{3EI}\left[1+3(1+\nu)\left(\frac{e}{L}\right)^2\right] \tag{4}$$

Where,

E = Young's modulus
I = The second moment of inertia of the hollow steel tubular cross-section
r = Radius of gyration of the hollow steel tubular cross-section
v = Poisson's ratio
σ_y = Yield strength

The steel is of Type Q345 in accordance with the Chinese standards: material properties such as its yield strength σ_y, ultimate strength σ_u, Young's modulus E, and Poisson's ratio v are 347 MPa, 506 MPa, 218 GPa, and 0.28, respectively. The concrete is a C50 grade where the compressive strength σ_{cu}, Young's modulus E_c, and Poisson's ratio v are 51 MPa, 31.062 GPa, and 0.20 (listed in Table 2), respectively.

2.2 Test Set-Up

Figure 3 shows the loading device: the eccentric vertical load, which is assumed as dead load of superstructure and vehicle load, was applied by 600 kN capacity hydraulic jacks connected to a self-reaction frame, meanwhile a sliding track was placed between the jack and the frame to ensure that the system remained upright under horizontal displacement of the top of the specimen. Horizontal cyclic loading, which is assumed as seismic load, was applied by a 500 kN hydraulic servo actuator installed on the counter-force wall. These axial and horizontal loads were applied to the specimen through a connecting component, which is the blue part shown in Fig. 3(a). During the loading process, to protect the hydraulic jacks and coordinate all in-plane deformation caused by the axial load and out-of-plane horizontal load, a circular rubber bearing was placed between the jack and the connecting component. A stiffening girder on the bottom of each specimen was bolted to the ground foundation to provide base fixity.

2.3 The Applied Load and Measuring Scheme

The loading was applied as follows: at eccentricity e from the axis of the column specimen to its point of action, a constant vertical load is transmitted through the connecting component. Then a stepwise increasing horizontal cyclic displacement step along the out-of-plane direction is applied in the same position. The incremental displacement was set to half the theoretical yield displacement δ_y, as shown in Fig. 4. The experiment was terminated, until the load bearing capacity dropped to 85% of its maximum value.

During the experiment, to avoid error arising from the design of the set-up and its deformation, six displacement sensors (two 200 mm stroke, two 100 mm stroke, and two 50 mm stroke) were installed on the sides of the connecting component, the stiffening girder, and the rubber bearing, separately, as shown in Fig. 5. The out-of-plane displacement δ and in-plane displacement δ_{in} of the specimen can be calculated by using Eqs. (5) and (6), respectively.

$$\delta = \delta_1 - \delta_2 - \frac{\delta_3 - \delta_4}{\mathrm{D}} \times \mathrm{L} \tag{5}$$

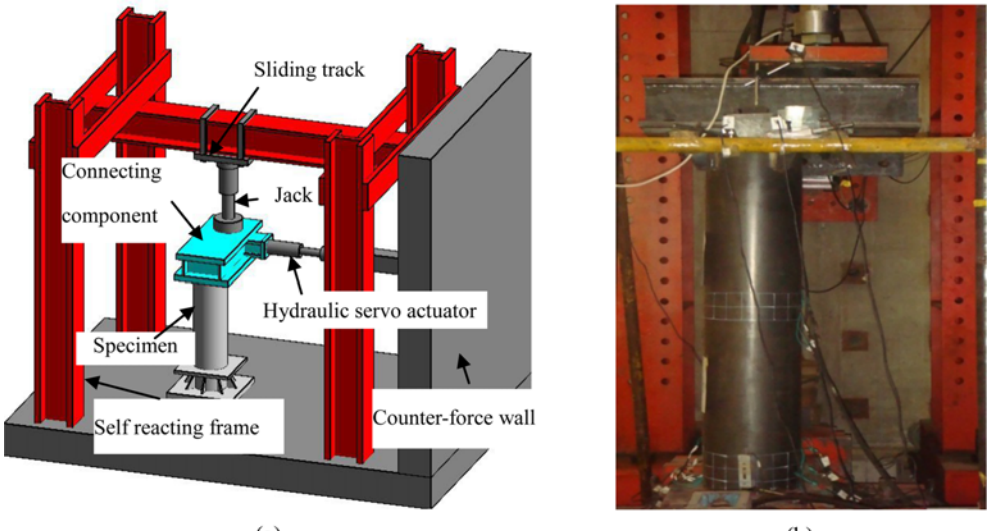

Fig. 3. Experimental Set-Up: (a) Sketch of the Test Set-Up, (b) On-Site Test Set-Up Photograph

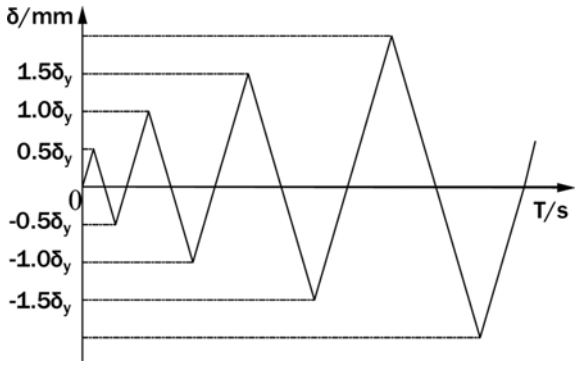

Fig. 4. The Out-of-Plane Horizontal Loading Protocol

$$\delta_{in} = \delta_6 - \delta_5 \tag{6}$$

Where,

D = Horizontal distance between the inward and outward axial displacement sensors

δ_1 = Out-of-plane horizontal displacement of the connecting component

δ_2 = Out-of-plane horizontal displacement at the bottom of the stiffening girder

δ_3 and δ_4 = Inward and outward vertical displacement of the ring-shaped stiffening girder

δ_5 = In-plane horizontal displacement at the bottom of the stiffening girder

δ_6 = In-plane horizontal displacement of the connecting component.

2.4 Finite Element Analysis Model

To investigate the failure mechanism of typical piers, four experimental specimens were analyzed by using the ABAQUS package. In recent years, in order to improve the accuracy and calculation efficiency of finite element analysis, several researchers have proposed calculation methods based on different theories and constitutive relationships of materials (Rahmzadeh et al., 2018; Bayat et al., 2019; Lyu et al., 2020). In this study, the modified Newton-Raphson algorithm was used for elasto-plastic analysis.

The constitutive model of steel is a bi-linear stress-strain relationship, the yield strength, Young's modulus and Poisson's ratio of steel adopted material tension test results, the secondary stiffness considered as 1/100 of the initial stiffness, the yield criterion used Von Mises yield criterion, the kinematic hardening model used which considers the Bauschinger effect. The concrete damage plasticity model is used for in-filled concrete (Goto et al., 2014). The compressive strength, tensile strength, elastic modulus and Poisson's ratio of concrete adopted the values of cubic compression material test. The other parameters used the default values in ABAQUS.

The finite element analysis (FEA) model is shown in Fig. 6. The loading conditions of the FEA model are consistent with the loading conditions of the test, and the boundary conditions are completely fixed at the bottom of the FEA model. In the analytical model, considering both the computation time and the accuracy of the FE model, the upper part of the steel tubular bridge pier was simplified as a type-B31 beam element. Some 24 beam elements were used (four for the cantilever beam and 20 for the upper part of the steel tube). The lower part of the steel tubular component, where large local buckling deformations may occur, was simulated by the square S4R-type of shell element. The mesh used to model the tube, along the perimeter direction, was divided into 36 elements, and along the longitudinal direction it was refined such that the refined concrete-filled segment and hollow segment height is only two thirds of the diameter of the steel tube with a refined element aspect ratio of 3:1. The in-filled concrete is simulated by C3D8R solid elements: the mesh used to model the concrete, along the radius, was divided into six elements. From the inside out, along the longitudinal direction, it was divided in the same way as the steel tube mesh.

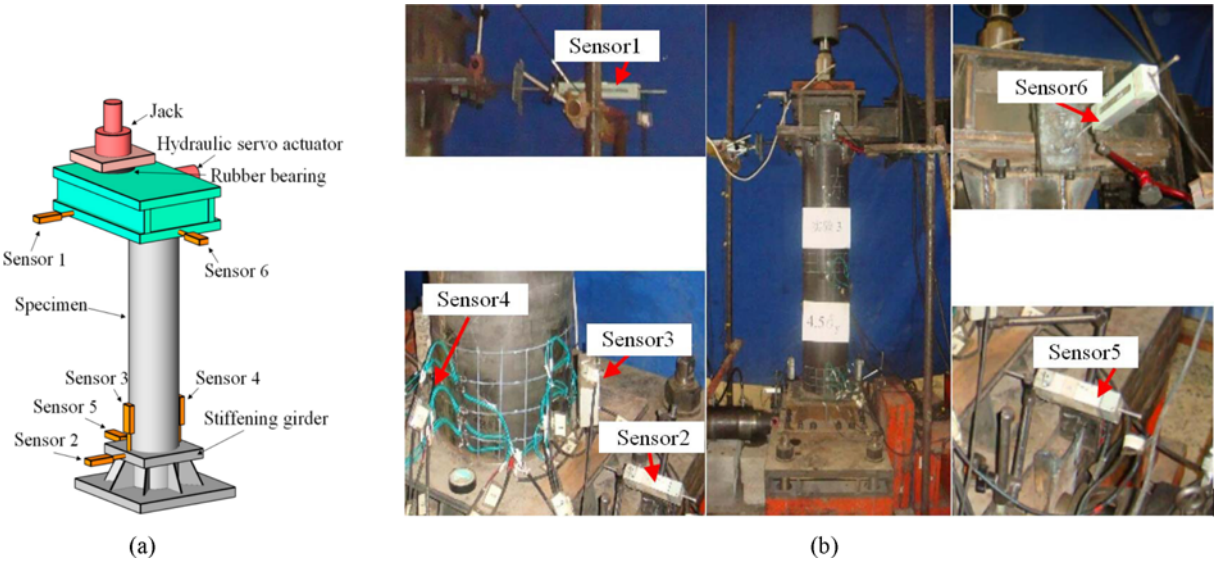

Fig. 5. Experimental Set-Up: (a) Position of the Displacement Sensor, (b) Displacement Sensor Arrangement

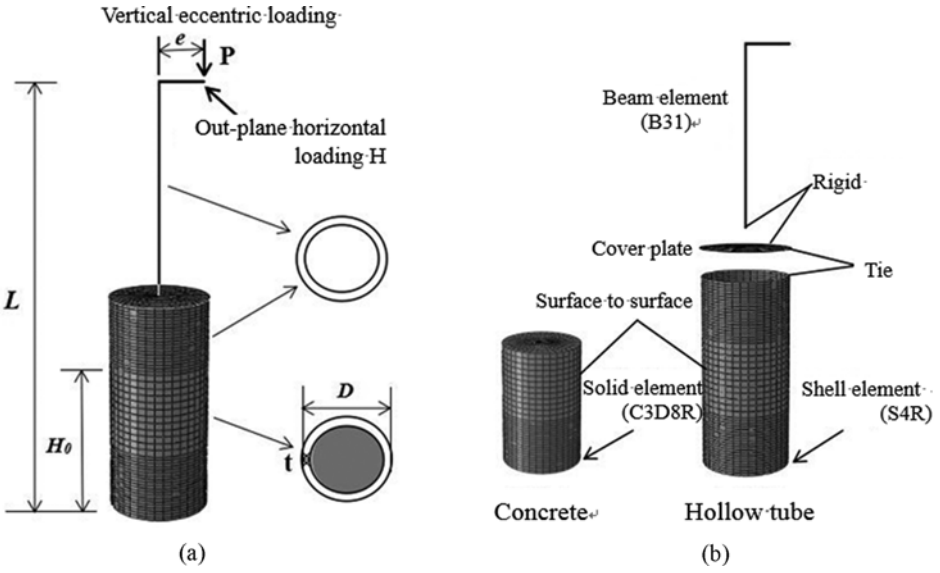

Fig. 6. Analytical Model: (a) Simplified Model of Bridge Pier, (b) Element Type Selection and Division

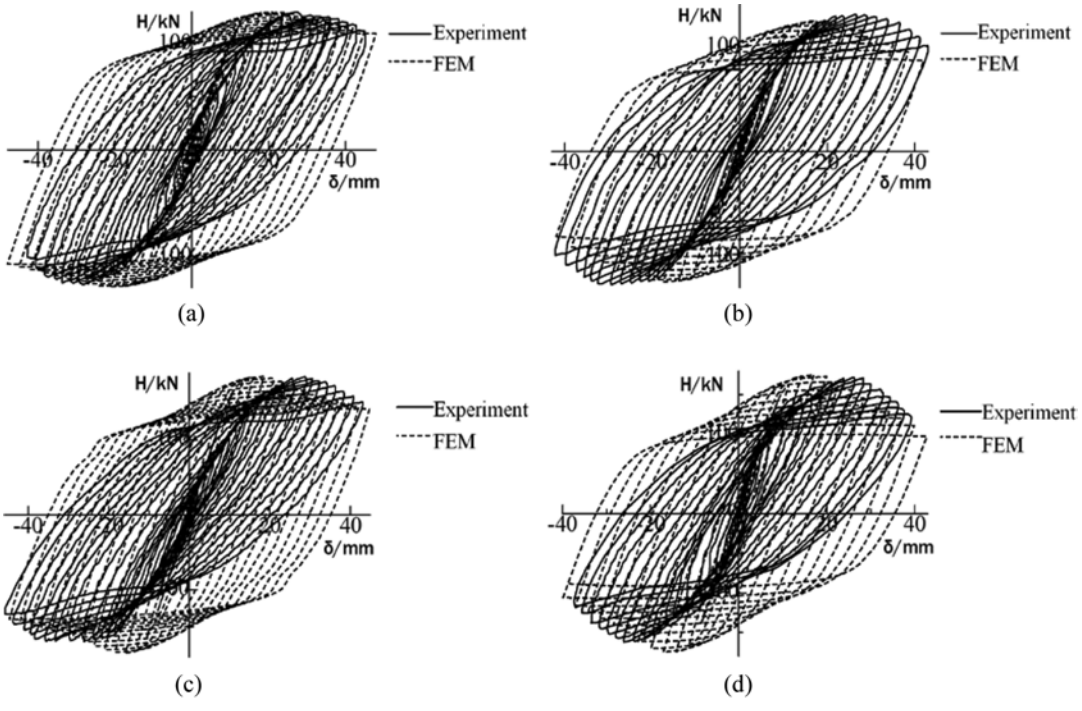

Fig. 7. Comparison of Analytical and Experimental Out-of-Plane Horizontal Load-Displacement Hysteresis Curves: (a) SCP1, (b) SCP2, (c) SCP3, (d) SCP4

A rigid body was used to connect the upper simplified beam element and the lower shell element. The connection between the rigid body and the lower shell element was defined as a tie connection, and the contact between the lower part of the steel tubular part and the concrete was defined as a surface-to-surface contact.

When two surfaces between the lower shell element and solid element come into contact, a contact pressure acts on the respective surfaces. This contact pressure was herein calculated by using the hard contact model. When the two surfaces come into contact, frictional stress is generated in the direction tangential to the contact surface. This frictional behaviour can be expressed by the Coulomb friction model. The resultant shear stress $\tau_\Sigma = (\tau_1 + \tau_2)^{1/2}$ was calculated from the two orthogonal components of the shear stresses τ_1 and τ_2. The contact surfaces can carry the resultant shear stress τ_Σ up to the critical shear stress τ_{cr} before they start to slip. The critical shear stress τ_{cr} is proportional to the contact pressure f and is expressed as:

$$\tau_{cr} = \mu f \tag{7}$$

where μ is the friction coefficient (here, $\mu = 0.6$) (Rabbat and Russell, 1985; BaItay and Gjelsvik, 1990). If $\tau_\Sigma < \tau_{cr}$, no slip

Table 3. Comparisons of FE Analytical and Experimental Results

Specimen	H_y/kN	δ_y/mm	Analytical results		Experimental results		H_{max}/H_{max}'	$\delta_{max}/\delta_{max}'$
			H_{max}/kN	δ_{max}/ mm	H_{max}'/kN	δ_{max}'/mm		
SCP1	66.9	7.0	129.1	23.96	129.6	27.45	1.00	0.87
			-128.3	-23.84	-127.0	-28.74	1.01	0.83
SCP2	59.5	6.0	124.5	21.00	130.8	26.53	0.95	0.79
			-122.4	-21.00	-126.4	-27.06	0.97	0.78
SCP3	95.1	5.7	182.7	21.04	185.1	25.64	0.99	0.73
			-180.3	-21.04	-168.1	-29.52	1.07	0.71
SCP4	91.1	5.3	172.9	19.82	170.5	23.81	1.01	0.83
			-170.2	-19.95	-163.1	-26.05	1.04	0.77

Note: H_y and δ_y is the theoretical horizontal yield strength and the theoretical horizontal yield displacement, respectively; H_{max} is the analytical maximum strength, δ_{max} is the analytical horizontal displacement corresponding to H_{max}; H_{max}' is the experimental maximum strength; δ_{max}' is the experimental horizontal displacement corresponding to H_{max}'.

displacement occurs between the contact surfaces: if $\tau_\Sigma \geq \tau_{cr}$, slip should occur.

3. Experimental and Numerical Results

3.1 Horizontal Force-Displacement Hysteresis Curves

Figure 7 shows the experimental and analytical out-of-plane horizontal load-displacement hysteresis curve of the PCFST columns. In Fig. 7, the horizontal axis indicates the horizontal displacement, the vertical axis shows the horizontal force, the solid lines show analytical results, and the dashed lines are experimental results ("+" represent the Hydraulic servo actuator pull direction, "-" represent the Hydraulic servo actuator push direction).

Based on strain gauge measurements, the yielding of steel tubes in specimen SCP1 occurs at +13.47 mm (or -14.69 mm). When a displacement of +27.45 mm, the specimen reaches a maximum reaction force of +129.6 kN (or -127.0 kN), local buckling phenomenon observed at the bottom of the column. In specimen SCP2, the yielding of the steel tube occurs at +12.23 mm (or -13.36 mm), local buckling phenomenon observed at the bottom of the column after a displacement of +27.30 mm, and the specimen reaches a maximum reaction force of +130.8 kN (or -126.4 kN). The yielding of the steel in specimen SCP3 occurs at +14.46 mm (or -15.98 mm), and the maximum reaction force reaches +185.1 kN (or -168.1 kN). In specimen SCP4, yielding of the steel tubes occurs at +13.46 mm (or -14.37 mm), the maximum reaction force reaches +170.5 kN (or -163.1 kN). No cracking, or fracturing, of these four specimens was observed.

From the Fig. 7, it could be found that the FEA accurately simulated the mechanical behaviour of these steel tubular columns with partial concrete in-fill; although in the unloading process, the stiffness predicted by the FEA is greater than that measured experimentally. There are two reasons for this: 1) the in-filled concrete, in these specimens under cyclic loading, is crushed resulting in a reduction of the local stable bearing capacity of the steel tube, which leads to the rapid decline in stiffness in the experiment. In the FEA, however, the concrete is not rendered ineffective, even if it reaches its ultimate limit state, it exerts no influence on the local stable bearing capacity of the steel tube; 2) in these analyses, the steel material properties are simplified to a bi-linear stress-strain relationship resulting in excessive residual deformation. Based on the data in Table 3, the maximum deviation of the maximum horizontal force and the corresponding deformation are 5% and 30%, respectively.

3.2 Failure States of These Specimens

The failure modes of these experimental specimens, and the corresponding FEA results, are shown in Fig. 8. The local buckling position in the output from the FEA model is consistent with that observed experimentally, and the high-PEEQ (equivalent plastic strain) distribution region of the concrete coincides with the locus of the damage observed experimentally.

3.3 In-Plane Horizontal Displacement

Figure 9 shows the analytical and experimental in-plane horizontal displacement δ_{in} (as calculated by Eq. (6)) and out-of-plane horizontal displacement δ curves for the four specimens. Fig. 9(a) shows the hysteresis results and Fig. 9(b) shows the skeleton curve: as the out-of-plane horizontal displacement increased, the in-plane horizontal displacement increased linearly until δ reached 17.12 mm, 16.43 mm, -25.07 mm, and -20.06 mm for SCP1, SCP2, SCP3, and SCP4, respectively. The increase in δ_{in} was non-linear and the FEA, and experimental, results were in good agreement.

From the discussion, the validity and effectiveness of the numerical analysis were thus demonstrated.

4. Numerical Analyses

4.1 Illustration of Analytical Model

To study the effect of the vertical eccentric loading on the seismic performance of a PCFST bridge pier, 30 FE models, where, λ is 0.25, 0.3, and 0.35, R_t is 0.06, 0.08, 0.10 and 0.12, and

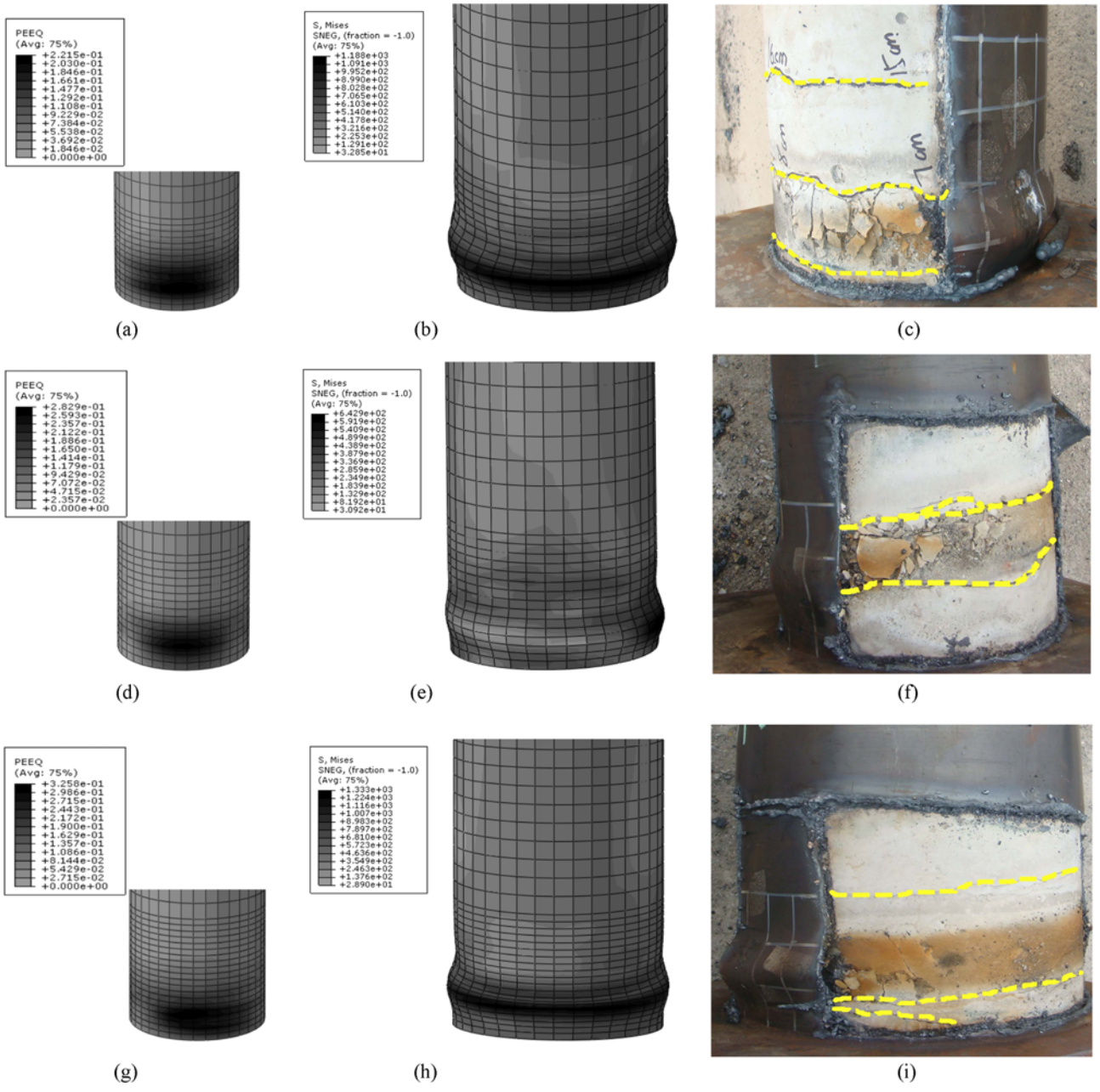

Fig. 8. Final Failure States of the Four FEA Models Compared with Their Experimental Counterparts:(a) Stress Distribution and Local Buckling of Model SCP1 (concrete), (b) Stress Distribution and Local Buckling of Model SCP1 (steel tube), (c) Failure Mode of Specimen SCP1, (d) Stress Distribution and Local Buckling of Model SCP2 (concrete), (e) Stress Distribution and Local Buckling of Model SCP2 (steel tube), (f) Failure Mode of Specimen SCP2, (g) Stress Distribution and Local Buckling of Model SCP3 (concrete), (h) Stress Distribution and Local Buckling of Model SCP3 (steel tube), (i) Failure Mode of Specimen SCP3, (j) Stress Distribution and Local Buckling of Model SCP4 (concrete), (k) Stress Distribution and Local Buckling of Model SCP4 (steel tube), (l) Failure Mode of Specimen SCP4

e/L is 0.00, 0.05, 0.10, 0.15, and 0.20, are established. The geometrical dimensions and parameters of the models are summarized in Table 4.

4.2 Effect of Parameters on Hysteretic Mechanical Behaviour

Horizontal force-displacement hysteresis curves of the five models in SCP30-06 series are shown in Fig. 10. Fig. 10 represents results of the five models with eccentricity ratio e/L = 0.00, 0.05, 0.10, 0.15, and 0.20, respectively. The horizontal axis indicates the horizontal non-dimensional displacement δ/δ_y and the vertical axis shows the horizontal non-dimensional force H/H_y along the out-of-plane horizontal direction.

It was found that the reaction force increased linearly as the horizontal displacement increased at the beginning of the loading phase, and after the displacement exceeded the yield displacement,

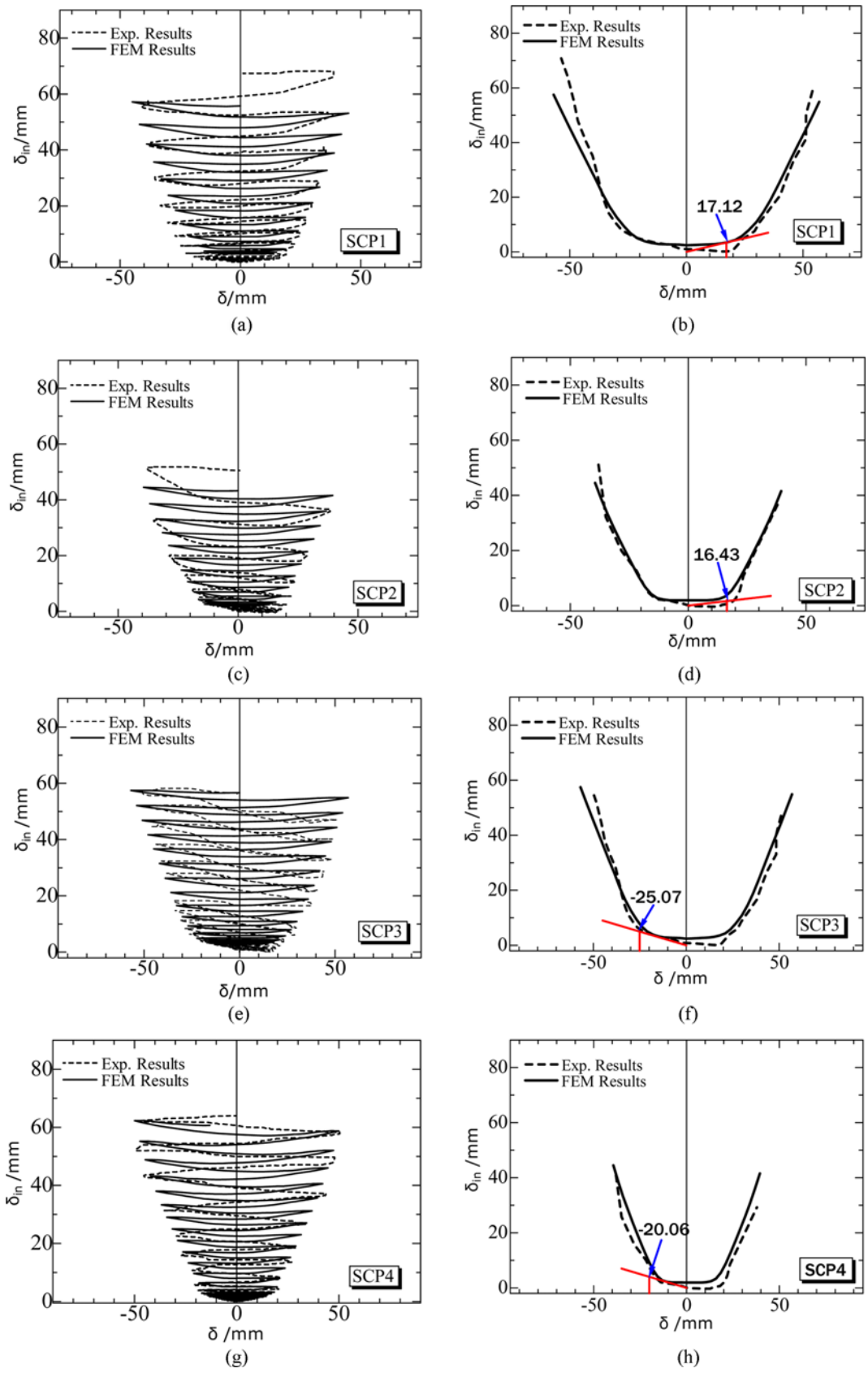

Fig. 9. The Analytical and Experimental In-plane Horizontal Displacement δ_{in} - Out-of-Plane Horizontal Displacement δ Curve: (a) Hysteresis Curve δ_{in}–δ of SCP1, (b) Skeleton Curve δ_{in}–δ of Model SCP1, (c) Hysteresis Curve δ_{in}–δ of SCP2, (d) Skeleton Curve δ_{in}–δ of Model SCP2, (e) Hysteresis Curve δ_{in}–δ of SCP3, (f) Skeleton Curve δ_{in}–δ of Model SCP3, (g) Hysteresis Curve δ_{in}–δ of SCP4, (h) Skeleton Curve δ_{in}–δ of Model SCP4

Table 4. Model Dimensions and Other Parameters

Model	L/mm	t/mm	λ	R_t	$\zeta = H_0/L$	P/ kN	e/L	H_y/kN	δ_y/mm
SCP30-06-00	17,000	70	0.30	0.06	0.22	33,344	0.00	7,952	91.4
SCP30-06-05							0.05	6,285	73.0
SCP30-06-10							0.10	4,618	55.1
SCP30-06-15							0.15	2,951	36.9
SCP30-06-20							0.20	1,283	17.0
SCP30-08-00	17,000	52	0.30	0.08	0.24	24,922	0.00	6,015	91.4
SCP30-08-05							0.05	4,769	73.2
SCP30-08-10							0.10	3,523	55.6
SCP30-08-15							0.15	2,277	37.6
SCP30-08-20							0.20	1,031	18.0
SCP30-10-00	17,000	42	0.30	0.10	0.26	20,198	0.00	4,908	91.4
SCP30-10-05							0.05	3,898	73.3
SCP30-10-10							0.10	2,888	55.9
SCP30-10-15							0.15	1,878	38.0
SCP30-10-20							0.20	868	18.7
SCP30-12-00	17,000	35	0.30	0.12	0.28	16,871	0.00	4,119	91.4
SCP30-12-05							0.05	3,275	73.4
SCP30-12-10							0.10	2,431	56.1
SCP30-12-15							0.15	1,588	38.3
SCP30-12-20							0.20	745	19.1
SCP25-10-00	14,300	42	0.25	0.10	0.34	20,198	0.00	5,834	64.7
SCP25-10-05							0.05	4,824	54.0
SCP25-10-10							0.10	3,817	43.9
SCP25-10-15							0.15	2,805	33.8
SCP25-10-20							0.20	1,795	23.0
SCP35-10-00	20,000	42	0.35	0.10	0.32	20,198	0.00	4,172	126.5
SCP35-10-05							0.05	3,162	96.8
SCP35-10-10							0.10	2,152	67.8
SCP35-10-15							0.15	1,142	37.6
SCP35-10-20							0.20	132	4.6

Note: Model name SCP indicates concrete-filled steel piers, the first two digits represent the column slenderness ratio, the middle two digits represent the radius-thickness ratio, and the final two represent the eccentricity ratio of that model.

the reaction force increased slowly. When the reaction force reached the maximum bearing capacity of the model, due to local buckling deformation at the bottom, the bearing capacity began to decrease quickly and the hysteretic performance was poorer as the eccentricity ratio increased. Regarding the limit state of bridge pier, several references have given accepted criteria for the limit state for the bridge pier (Usami and Ge, 1994; Chen and Duan, 2014; Goto et al., 2015). According to the 2018 JRA code (Japan Road Association, 2018), the maximum bearing capacity of a pier is defined as the ultimate strength of the pier, and the corresponding displacement is the ductility of the pier.

Figure 11 shows horizontal force-displacement skeleton curves of the 30 FE models. The initial stiffness of the five specimens in each series are generally in agreement as shown in Fig. 11. This indicates that the vertical load eccentricity ratio e/L has little influence on the initial stiffness of the specimens in the range $0 \leq e/L \leq 0.2$. After entering the elasto-plastic stage, with increasing vertical load eccentricity, the ultimate strength of the model in each group decreases gradually. After the ultimate strength is reached, the descent speed of the curve is gradually accelerated, and the ductility diminishes. It is found that the skeleton curve before reaching the ultimate strength of the model with a small vertical load eccentricity (e.g., $e/L = 0.05$) is similar to that of a non-eccentric model. After reaching the ultimate strength, the curve falls slowly, indicating good ductility; however, when the vertical load eccentricity is greater (e.g., $e/L = 0.20$), the ultimate strength of the model is reduced greatly compared with that of the non-eccentric model, and the rate of descent of the curve after reaching the ultimate strength is accelerated.

4.3 Single-Parameter Analysis

To quantify the influence of the radius-thickness ratio R_t, slenderness ratio λ, and other design parameters on the seismic performance

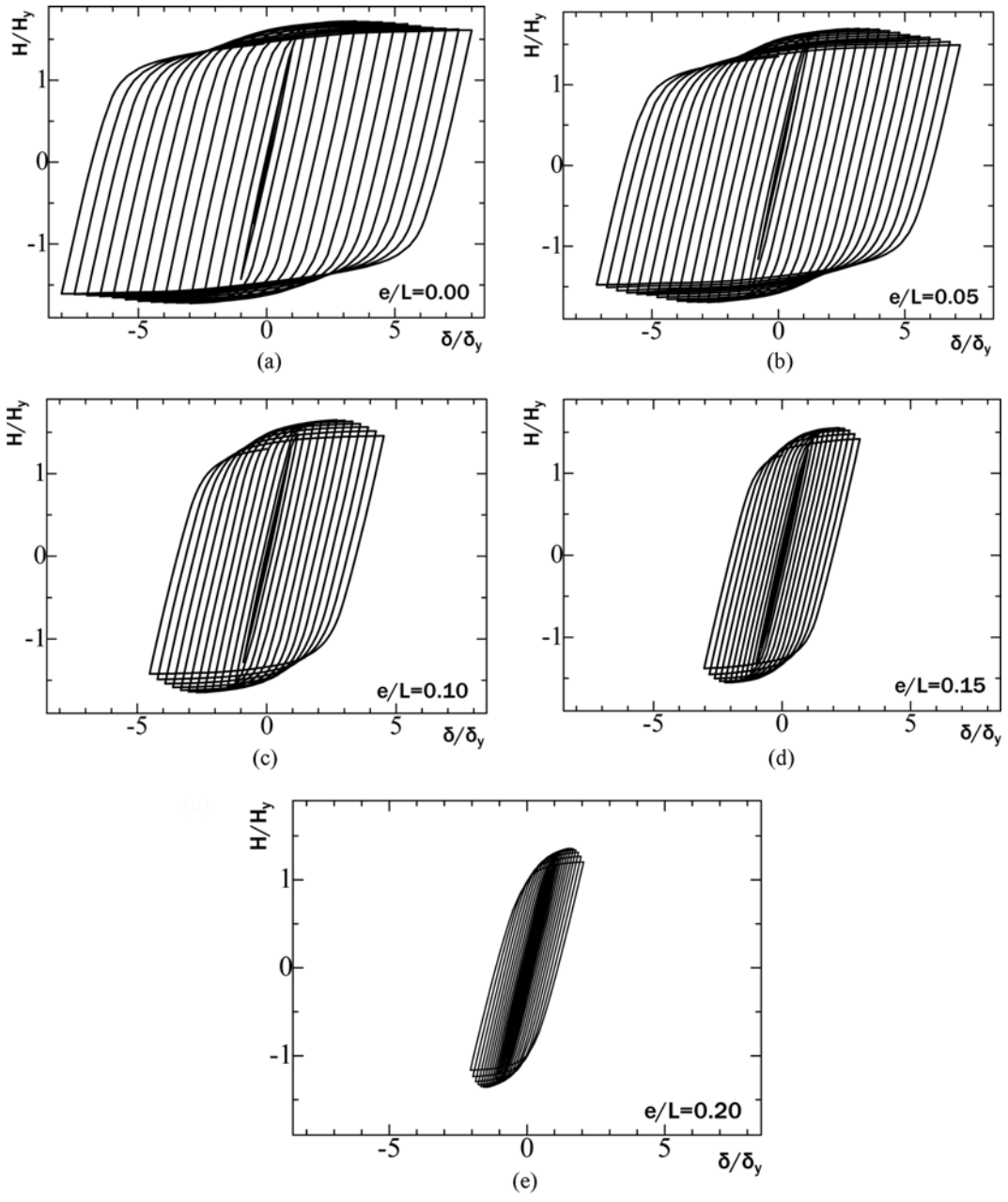

Fig. 10. Horizontal Force-Displacement Hysteretic Curves of These Five Models SCP30-06 Series: (a) SCP30-06-00, (b) SCP30-06-05, (c) SCP30-06-10, (d) SCP30-06-15, (e) SCP30-06-20

of this type of bridge pier, a single-parameter analysis is carried out on the ultimate strength and ductility obtained from the 30 FE models.

At a slenderness ratio λ of 0.30, the vertical load eccentricity e/L varies from 0 to 0.20, the influence of the radius-thickness ratio R_t on the ultimate strength and displacement ductility of the bridge piers is shown in Fig. 12. Fig. 12(a) shows the relationship between the ultimate strength H_u/H_y and R_t. Fig. 12(b) shows the relationship between displacement ductility δ_u/δ_y and R_t. Fig. 12(c) shows the relationship of δ_u/δ_y-H_u/H_y-R_t. Here, to facilitate comparison, displacement ductility is defined as the ratio of the horizontal ultimate displacement of bridge pier to the horizontal yield displacement of a vertical, non-eccentrically loaded, bridge pier. The horizontal ultimate displacement is the displacement corresponding to the ultimate strength.

In the case of identical eccentricity ratio, with the increase of radius-thickness ratio R_t, the ultimate strength increases gradually, except for the bridge pier with $R_t = 0.12$ and $e/L = 0.20$. For a given R_t, with increased vertical load eccentricity, the ultimate strength of the bridge pier gradually decreases; when the eccentricity ratio e/L changes from 0.15 to 0.20, the ultimate strength of the bridge pier decreases rapidly, and when e/L is increased from 0 to 0.2, the ultimate strength has decreased by an average of 24% (see Fig. 12(a)). When the eccentricity ratio e/L

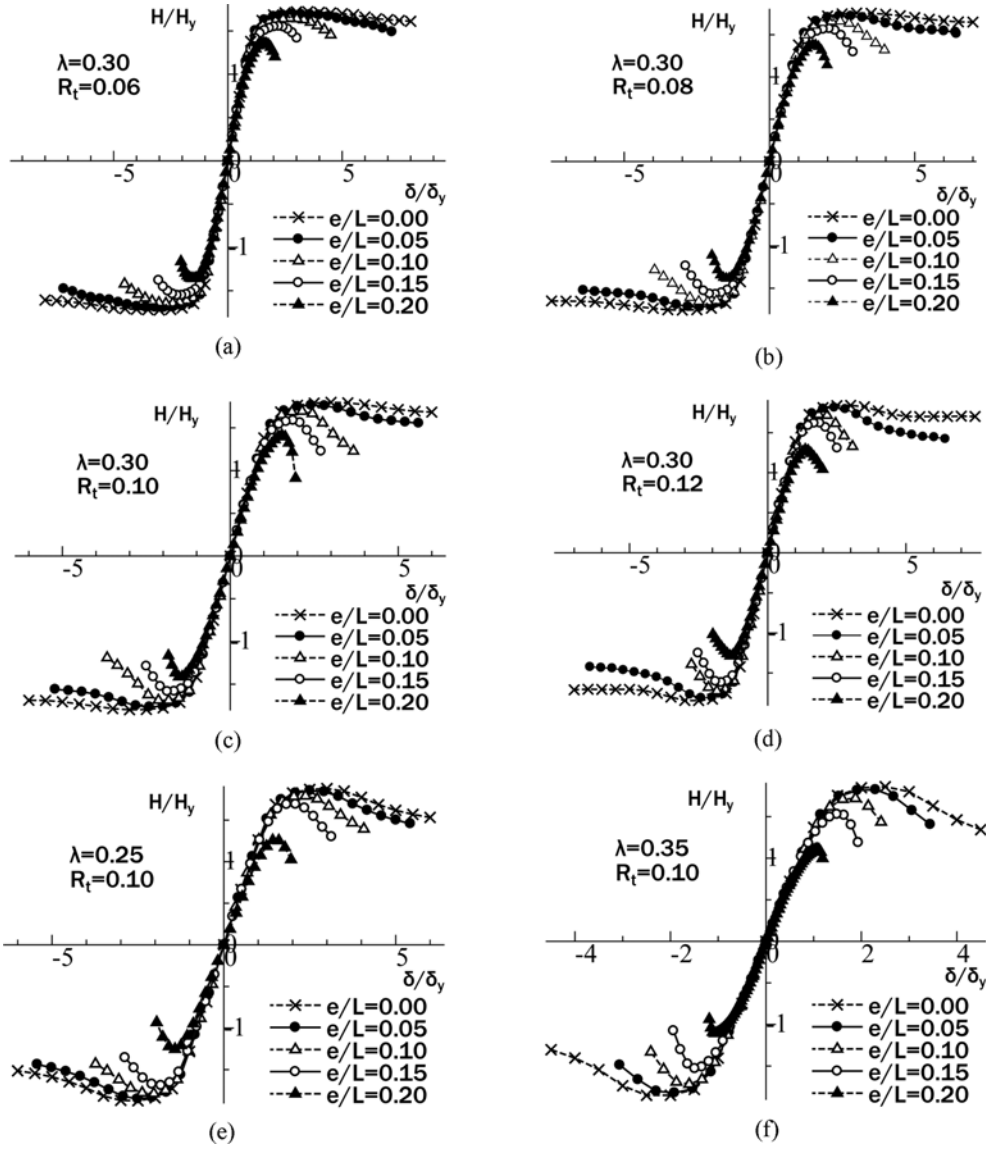

Fig. 11. Horizontal Force-Displacement Skeleton Curves: (a) SCP30-06 Series, (b) SCP30-08 Series, (c) SCP30-10 Series, (d) SCP30-12 Series, (e) SCP25-10 Series, (f) SCP35-10 Series

is constant, with increasing R_t, the displacement ductility of the pier gradually decreases. For a given R_t, with an increased e/L ratio, the displacement ductility of the pier gradually decreases; when e/L increases from 0 to 0.2, the displacement ductility decreases by more than 50% (Fig. 12(b)).

When the radius-thickness ratio R_t is 0.10, and the vertical load eccentricity e/L is varied from 0 to 0.20, the influence of the slenderness ratio λ on the ultimate strength and displacement ductility of the bridge piers is as shown in Fig. 13.

For a constant e/L ratio, the ultimate strength of each bridge pier decreases gradually with increasing slenderness ratio λ except for the pier with $\lambda = 0.30$, and $e/L = 0.20$. At constant λ, with the increase of e/L, the ultimate strength of the bridge pier decreases; when e/L is varied from 0.15 to 0.20, the ultimate strength of the bridge pier decreases rapidly; as e/L increases from 0 to 0.2, the ultimate strength decreases by an average of more than 24%. When e/L is constant, with increasing λ, the displacement ductility of the pier gradually decreases. For a constant λ, with increasing e/L, the displacement ductility of the pier gradually decreases; when e/L is increased from 0 to 0.2, the displacement ductility decreases by an average of 50%.

4.4 Establish of an Empirical Formula and Its Validation

Through the analysis of the slenderness ratio λ and radius-thickness ratio R_t effects on the ultimate strength and displacement ductility of the bridge piers, it can be found that, with increased vertical load eccentricity, the ultimate strength or the displacement ductility of the bridge pier is independent of that of the same bridge pier under vertical non-eccentric loading. When the design parameters of the bridge piers are the same, the vertical load eccentricity can be considered as the main factor that affects the seismic performance of this type of bridge pier. Thus, based on

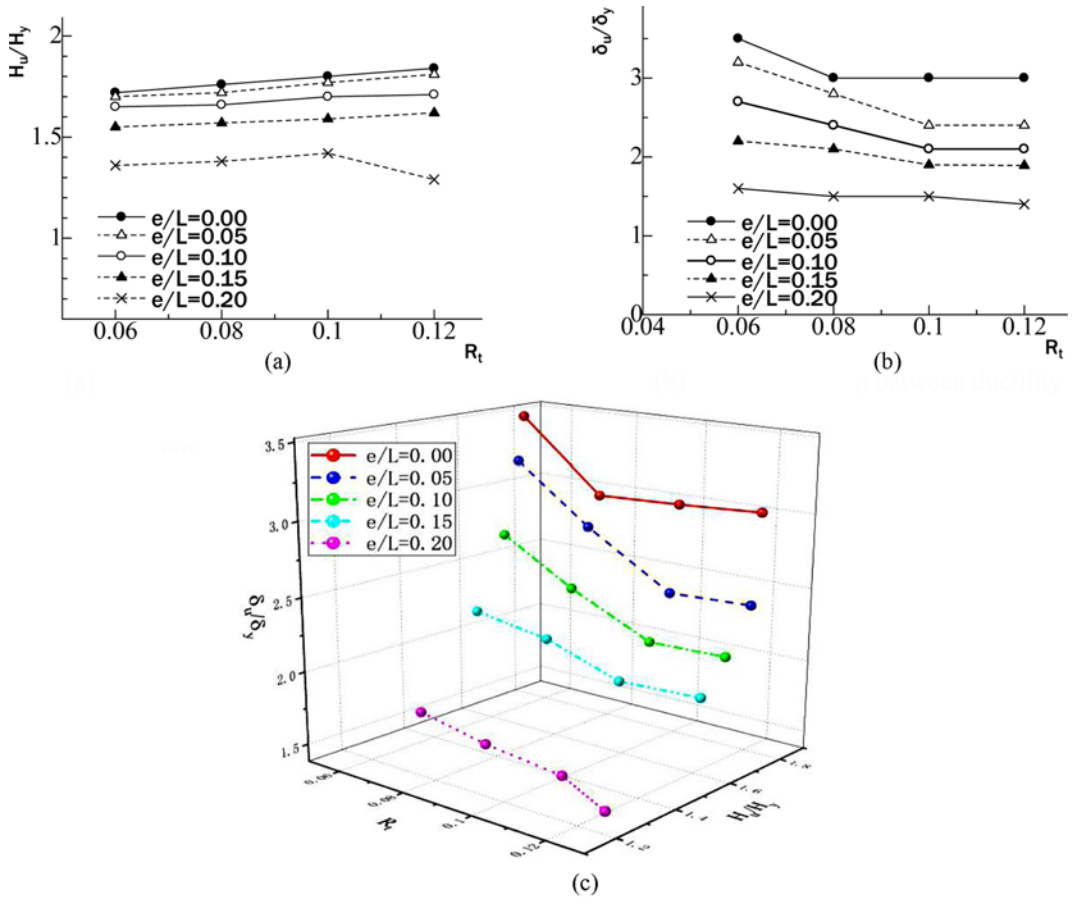

Fig. 12. The Relationship between Bearing Capacity and Ductility for Different Radius-Thickness Ratios R_t: (a) The Relationship between Bearing Capacity and Radius-Thickness Ratio R_t, (b) The Relationship between Ductility and Radius-Thickness Ratio R_t, (c) The Relationship of δ_u/δ_y - H_u/H_y - R_t

the influence of the slenderness ratio λ and radius-thickness ratio R_t on the ultimate strength and displacement ductility of the centrally loaded PCFST bridge pier (Wang et al., 2015), the vertical load eccentricity is taken as the key parameter when considering the influence of eccentricity ratio on the ultimate strength and displacement ductility of a bridge pier. Finally, an empirical formula for the ultimate strength and displacement ductility of the bridge piers under vertical eccentric load is established.

The ultimate strength and displacement ductility of the bridge piers under vertical non-eccentric loading can be calculated by using Eqs. (8) and (9) (Wang et al., 2015): when Eqs. (8) and (9) are multiplied by the reduction coefficients γ_1 and γ_2, respectively, they form empirical formulae for the ultimate strength and displacement ductility of these bridge piers under vertical eccentric load (Eqs. (10) and (11), respectively). The reduction coefficients γ_1 and γ_2 are functions associated with the vertical load eccentricity.

$$\frac{H_u}{H_y}=\frac{3.06R_t^{0.09}}{\lambda^{0.15}}-1.3 \tag{8}$$

$$\frac{\delta_u}{\delta_y}=0.384\times\frac{833R_t^2-191.7R_t+17.5}{\lambda^{1.03}}-3.9 \tag{9}$$

$$\frac{H_u}{H_y}=\left(\frac{3.06R_t^{0.09}}{\lambda^{0.15}}-1.3\right)\times\gamma_1 \tag{10}$$

$$\frac{\delta_u}{\delta_y}=\left(0.384\times\frac{833R_t^2-191.7R_t+17.5}{\lambda^{1.03}}-3.9\right)\times\gamma_2 \tag{11}$$

Using FEA output from the 30 bridge piers (above), the relationship of γ_1 and γ_2 with the vertical load eccentricity is found to be as follows:

$$\gamma_1=\begin{cases}\left(e/L+0.86\right)^{-0.6} & \left(0\le e/L\le 0.15\right)\\ \left(e/L+0.94\right)^{-1.24} & \left(0.15<e/L\le 0.2\right)\end{cases} \tag{12}$$

$$\gamma_2=\left(0.72-e/L\right)^{2.4-\frac{R_t}{\lambda}}\quad\left(0\le e/L\le 0.2\right) \tag{13}$$

To verify the validity of the empirical formulae for the ultimate strength and ductility of the bridge piers under vertical eccentric load, a comparative analysis of the discrepancy between the theoretical ultimate strength and ductility of the bridge piers under vertical eccentric load is calculated by using Eqs. (10) to (13) and

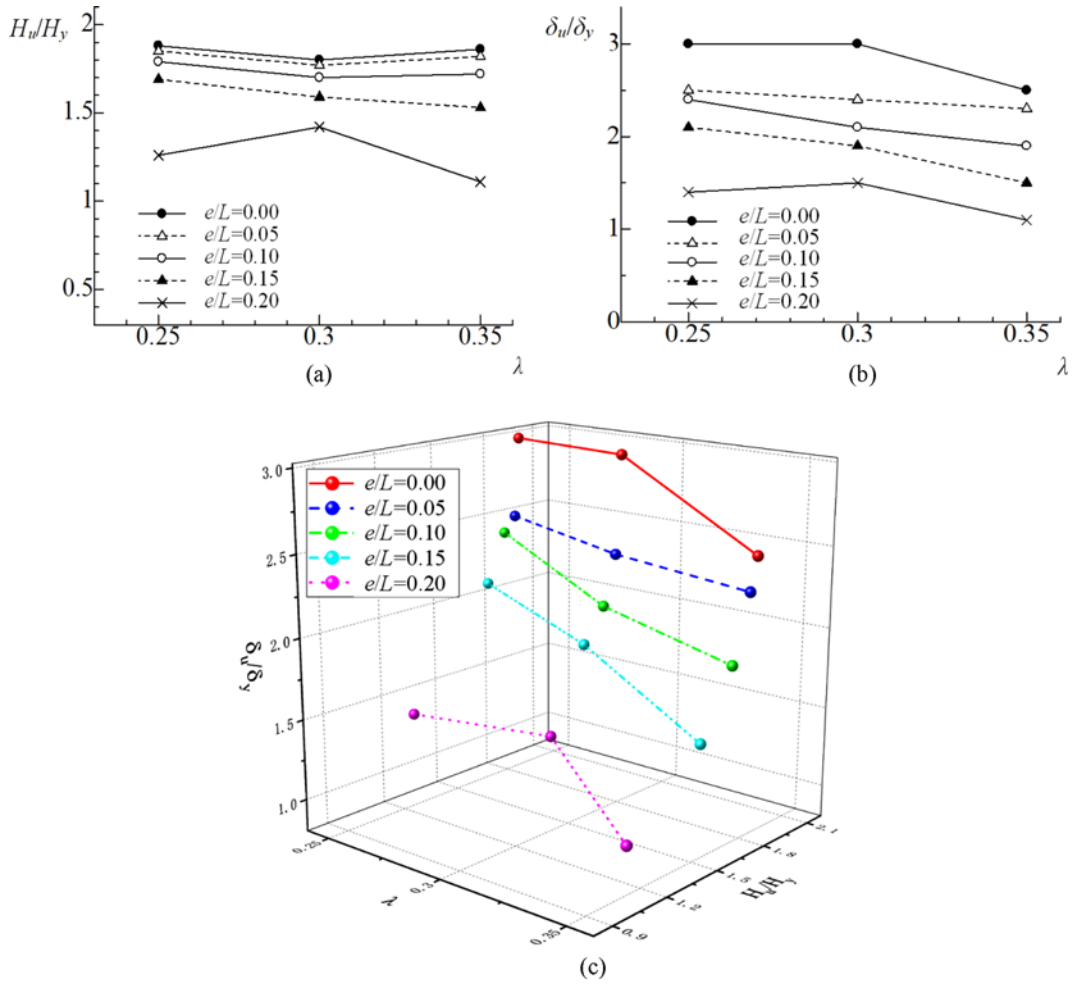

Fig. 13. The Relationships between Bearing Capacity and Ductility for Different Slenderness Ratios λ: (a) The Relationship between Bearing Capacity and Slenderness Ratio λ, (b) The Relationship between Ductility and Slenderness Ratio λ, (c) The Relationship of δ_u/δ_y - H_u/H_y - λ

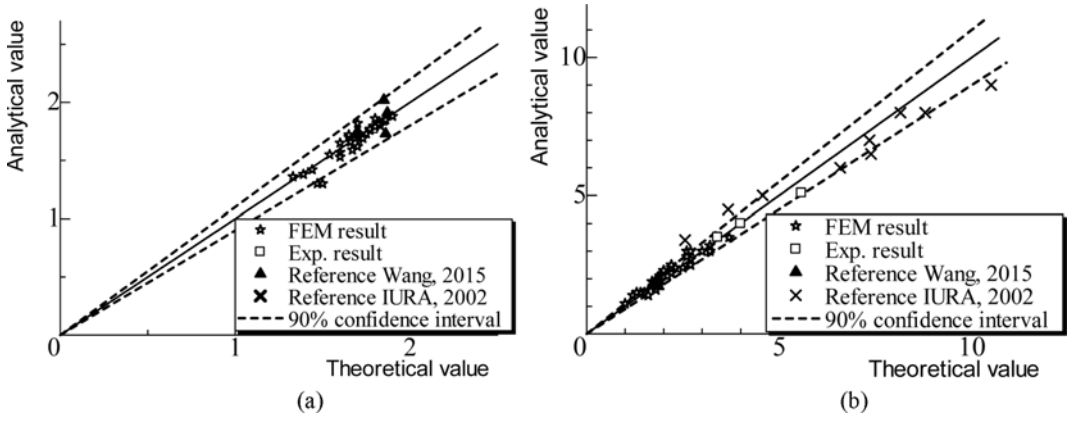

Fig. 14. Analysis of the Discrepancies between Theoretical, and Experimental, Values: (a) Maximum Bearing Capacity Formula, (b) Ductility Formula

the previous experimental results (see Fig. 14).

Both the ultimate strength and the ductility errors are in the vicinity of line $y = x$, and within the 90% confidence interval. The empirical formulae for the ultimate strength and the ductility of the bridge piers under vertical eccentric load are thus deemed accurate.

5. Conclusions

From the comparison of FEA, and experimental, results, regardless of the ultimate strength, the initial stiffness of the hysteresis curves, their final failure mode, and the deformation of the

specimens are in good agreement. This confirmed the validity of the FE model.

The vertical eccentric loading exerts a significant influence on the seismic performance of these PCFST bridge piers. With increasing eccentricity ratio *e/L*, the ultimate strength and ductility of the bridge piers decreases. When *e/L* increases from 0 to 0.2, the ultimate strength and ductility of bridge piers are reduced by 24% and 50%, respectively.

Based on a single-parameter analysis, the influence of vertical load eccentricity ratio *e/L*, as it was varied from 0 to 0.2, on the ultimate strength and ductility of these PCFST bridge piers along the out-of-plane horizontal direction is ascertained and the corresponding relationship between them proposed. The accuracy of the empirical formulae is verified and this research provides a theoretical basis for its application to this type of bridge pier.

Acknowledgements

This study was supported by the Project of the National Science and Technology Ministry 13th Five-Year Science and Technology (2017YFC0703805-03) and the Education Department Foundation of Liaoning Province in China (LN2019056), these supports are gratefully acknowledged.

ORCID

Not Applicable

References

Aoki T, Suzuki S, Watanabe S, Suzuki M, Usami T, Ge HB (2003) Experimental study on strength and deformation capacity of inverted *L*-shaped steel bridge piers subjected to out-of-plane cyclic loading. *Structural Engineering and Earthquake Engineering* 2003(724):213-223, DOI: 10.2208/jscej.2003.724_213 (in Japanese)

Baltay P, Gjelsvik A (1990) Coefficient of friction for steel on concrete at high normal stress. *Journal of Materials in Civil Engineering* 2(1):46-49, DOI: 10.1061/(ASCE)0899-1561(1990)2:1(46)

Bayat M, Ahmadi HR, Mahdavi N (2019) Application of power spectral density function for damage diagnosis of bridge piers. *Structural Engineering and Mechanics* 71(1):57-63, DOI: 10.12989/sem.2019.71.1.057

Chen WF, Duan L (2014) Bridge engineering handbook (second edition) - Seismic design. CRC Press Taylor & Francis Group, Boca Raton, FL, USA

Gao SB, Usami T, Ge HB (2000a) Eccentrically loaded steel columns under cyclic in-plane loading. *Journal of Structural Engineering* 126(8):964-973, DOI: 10.1061/(ASCE)0733-9445(2000)126:8(964)

Gao SB, Usami T, Ge HB (2000b) Eccentrically loaded steel columns under cyclic out-of-plane loading. *Journal of Structural Engineering* 126(8):974-981, DOI: 10.1061/(ASCE)0733-9445(2000)126:8(974)

Ge HB, Usami T (1996) Cyclic tests of concrete-filled steel box columns. *Journal of Structural Engineering* 122(10):1169-1177, DOI: 10.1061/(ASCE)0733-9445(1996)122:10(1169)

Ge HB, Watanabe S, Usami T, Aoki T (2003) Analytical study on strength and deformation capacity of inverted *L*-shaped steel bridge piers subjected to out-of-plane cyclic loading. *Structural Engineering and Earthquake Engineering* 738(64):207-218, DOI: 10.2208/jscej.2003.738_207 (in Japanese)

Goto Y, Ebisawa T, Lu XL (2014) Local buckling restraining behavior of thin-walled circular CFT columns under seismic loads. *Journal of Structural Engineering* 140(5):1-14, DOI: 10.1061/(ASCE)ST.1943-541X.0000904

Goto Y, Ebisawa T, Lu XL, Lu WS (2015) Ultimate state of thin-walled circular steel columns subjected to biaxial horizontal forces and biaxial bending moments caused by bidirectional seismic accelerations. *Journal of Structural Engineering* 141(4):04014122-1-12, DOI: 10.1061/(ASCE)ST.1943-541X.0001067

Goto Y, Kumar G, Kawanishi N (2010) Nonlinear finite-element analysis for hysteretic behavior of thin-walled circular steel columns with in-filled concrete. *Journal of Structural Engineering* 136(11):1413-1422, DOI: 10.1061/(ASCE)ST.1943-541X.0000240

Goto Y, Mizuno K, Prosenjit KG (2012) Nonlinear finite element analysis for cyclic behavior of thin-walled stiffened rectangular steel columns with in-filled concrete. *Journal of Structural Engineering* 138(5):571-584, DOI: 10.1061/(ASCE)ST.1943-541X.0000504

Hirota T, Yamao T, Tsumagari S, Sakimaoto T, Watanabe H (2005) Calculation formula for concrete filling rate of inverted L-shaped steel bridge piers. *Journal of Structural Engineering* 51A:149-161 (in Japanese)

Hua W, Wang HJ, Hasegawa A (2014) Experimental study on reinforced concrete filled circular steel tubular columns. *Steel & Composite Structures, an International Journal* 17(4):517-533, DOI: 10.12989/scs.2014.17.4.517

Iura M, Orino A, Ishizawa T (2002) Elasto-plastic behavior of concrete-filled steel tubular columns. *Structural Engineering and Earthquake Engineering* 696(58):285-298, DOI: 10.2208/jscej.2002.696_285 (in Japanese)

Japan Road Association (2018) Specification for highway bridges part v seismic design. Maruzen Co., Ltd., Tokyo, Japan

Japan Society of Civil Engineers (1996) Report on the Hanshin-Awaji earthquake disaster - Damage to civil engineering structures bridge structure. Maruzen Co., Ltd., Tokyo, Japan

Kim DW, Jeon CH, Shim CS (2016) Cyclic and static behaviors of CFT modular bridge pier with enhanced bracings. *Steel & Composite Structures* 20(6):1221-1236, DOI: 10.12989/scs.2016.20.6.1221

Kim DW, Shim CS (2016) Experiments on flexural strength on composite modular bridge pier cap for CFT columns. *KSCE Journal of Civil Engineering* 20(9):2483-2491, DOI: 10.1007/s12205-015-1467-9

Lyu F, Goto Y, Kawanishi N, Xu Y (2020) Three-dimensional numerical model for seismic analysis of bridge system with multiple thin-walled partially concrete-filled steel tubular columns. *Journal of Structural Engineering* 146(1):04019164-1-16, DOI: 10.1061/(ASCE)ST.1943-541X.0002451

Mahdavi N, Ahmadi HR, Bayat M (2019) Efficient parameters to predict the nonlinear behavior of FRP retrofitted RC columns. *Structural Engineering and Mechanics* 70(6):703-710, DOI: 10.12989/sem.2019.70.6.703

Michel B, Julia M (2004) Seismic design of concrete-filled circular steel bridge piers. *Journal of Bridge Engineering* 9(1):24-34, DOI: 10.1061/(ASCE)1084-0702(2004)9:1(24)

Nie JG, Wang YH, Fan JS (2012) Experimental study on seismic behavior of concrete filled steel tube columns under pure torsion and compression-torsion cyclic load. *Journal of Constructional Steel Research* 79:115-126, DOI: 10.1016/j.jcsr.2012.07.029

Nishikawa K, Yamamoto S, Natori T (1998) Retrofitting for seismic upgrading of steel bridge columns. *Engineering Structure* 20(4-6):540-551, DOI: 10.1016/S0141-0296(97)00025-4

Rabbat BG, Russell HG (1985) Friction coefficient of steel on concrete or grout. *Journal of Structural Engineering* 111(3):505-515, DOI: 10.1061/(ASCE)0733-9445(1985)111:3(505)

Rahmzadeh A, Alam MS, Tremblay R (2018) Analytical prediction and finite-element simulation of the lateral response of rocking steel bridge piers with energy-dissipating steel bars. *Journal of Structural Engineering* 144(11):04018210-1-15, DOI: 10.1061/(ASCE)ST.1943-541X.0002216

Sakimoto T, Nakayama M, Kawabata T, Watanabe H, Eyama E (2002) Hysteretic behavior of inverted L-shaped steel bridge piers subjected to out-of-plane cyclic loading. *Structural Engineering and Earthquake Engineering* 696(54):215-224, DOI: 10.2208/jscej.2002.696_215 (in Japanese)

Shimaguchi Y, Suzuki M (2015) Seismic performance evaluation of circular steel bridge piers which have damage and concrete filled repair. *Journal of Structural Engineering* 61A:292-301, DOI: 10.11532/structcivil.61A.292 (in Japanese)

Skalomenos KA, Hayashi K, Nishi R, Inamasu H, Nakashima M (2016) Experimental behavior of concrete-filled steel tube columns using ultrahigh-strength steel. *Journal of Structural Engineering* 142(9): 04016057-1-13, DOI: 10.1061/(ASCE)ST.1943-541X.0001513

Sui WN, Cheng HB, Wang ZF (2018) Bearing capacity of an eccentric tubular concrete-filled steel bridge pier. *Steel & Composite Structures, an International Journal* 27(3):285-295, DOI: 10.12989/scs.2018.27.3.285

Usami T, Ge HB (1994) Ductility of concrete-filled steel box columns under cyclic loading. *Journal of Structural Engineering* 120(7):2021-2040, DOI: 10.1061/(ASCE)0733-9445(1994)120:7(2021)

Usami T, Ge HB, Saizuka K (1997) Behavior of partially concrete-filled steel bridge piers under cyclic and dynamic loading. *Journal of Constructional Steel Research* 41(2):121-136, DOI: 10.1016/s0143-974x(97)00007-2

Wang ZF, Sui WN, Li GC, Wu Q, Ge L (2015) Mechanical behavior of partial concrete-filled steel circular bridge piers under cyclic lateral load. *China Journal of Highway and Transport* 28(1):62-70 (in Chinese)

Wang ZF, Wu Q, Sui WN (2011) Effect of filled-concrete height on ultimate strength and ductility of steel tubular bridge pier with partial filled-concrete. *Advanced Materials Research* 803-806:368-373, DOI: 10.4028/www.scientific.net/AMR.368-373.803

Wang ZF, Zhang X, Zhang ZJ, Li GC (2016) Study on hysteretic behavior of inverted-*L* shaped steel tubular bridge piers under out-of-plane cyclic loading. 11th pacific structural steel conference, October 26-28, Shanghai, China, 277-284

Yamao T, Iwatsubo K, Yamamuro T, Ogushi M, Matsumura S (2002) Steel bridge piers with inner cruciform plates under cyclic loading. *Thin-Walled Structures* 40(2):183-197, DOI: 10.1016/s0263-8231(01)00059-3

Zhao LD, Cao WL, Guo HZ, Zhao Y, Yang ZY (2018) Experimental and numerical analysis of large-scale circular concrete-filled steel tubular columns with various constructural measures under high axial load ratios. *Applied Sciences* 8(10):1894-1-21, DOI: 10.3390/app8101894